Physica Medica 62 (2019) 129–139

Contents lists available at ScienceDirect

Physica Medica

journal homepage: www.elsevier.com/locate/ejmp

Original paper

A rationale for cone beam CT with extended longitudinal field-of-view in image guided adaptive radiotherapy

K. Mohamathu Rafic*, S. Balasingh Timothy Peace, Mathew Manu, Sathyamurthy Arvind,
B. Paul Ravindran

Department of Radiation Oncology, Christian Medical College, Vellore 632004, Tamil Nadu, India

ABSTRACT

Purpose: To investigate the efficacy of using cone beam CT with extended longitudinal field-of-view ($\mathrm{CBCT}_{\mathrm{eLFOV}}$) for image guided adaptive radiotherapy (IGART).
Methods: The protocol acquires two CBCT scans with a linear translation of treatment couch in the patient plane, allowing a 1 cm penumbral overlap (i.e. cone beam abutment) and fused as a single DICOM set ($\mathrm{CBCT}_{\mathrm{eLFOV}}$) using a custom-developed software script (coded in MatLab®) for extended localization. Systemic validation was performed to evaluate the geometric and Hounsfield Units accuracy at the overlapping regions of the $\mathrm{CBCT}_{\mathrm{eLFOV}}$ using a Catphan®-504 phantom. Two case studies were used to illustrate the $\mathrm{CBCT}_{\mathrm{eLFOV}}$-based IGART workflow in terms of dosimetric and clinical perspectives. Segmentation accuracy/association between repeat CT (re-CT) and $\mathrm{CBCT}_{\mathrm{eLFOV}}$ was evaluated. Moreover, the efficacy of the $\mathrm{CBCT}_{\mathrm{eLFOV}}$ image data in deformable registration was also described.
Results: Slice geometry, spatial resolution, line profiles and HU accuracy in the overlapping regions of the $\mathrm{CBCT}_{\mathrm{eLFOV}}$ yielded identical results when compared with reference CBCT. In patient studies, the dice-similarity-coefficient evaluation showed a good association (> 0.9) between re-CT and $\mathrm{CBCT}_{\mathrm{eLFOV}}$. Dosimetric analysis of the $\mathrm{CBCT}_{\mathrm{eLFOV}}$-based adaptive re-plans showed excellent agreement with re-CT based re-plans. Moreover, a similar and consistent pattern of results was also observed using deformed image data (initial planning CT deformed to $\mathrm{CBCT}_{\mathrm{eLFOV}}$) with extended longitudinal projection and the same frame-of-reference as that of the $\mathrm{CBCT}_{\mathrm{eLFOV}}$.
Conclusion: Utilization of $\mathrm{CBCT}_{\mathrm{eLFOV}}$ proves to be clinically appropriate and enables accurate prediction of geometric and dosimetric consequences within the planned course of treatment. The ability to compute $\mathrm{CBCT}_{\mathrm{eLFOV}}$-based treatment plans equivalent to re-CT promises a potential improvement in IGART practice.

1. Introduction

A kilovoltage cone beam computed tomography (kV CBCT) system mounted on a modern linear accelerator enables acquisition of high-resolution volumetric images for online image guidance and target localization [1,2]. This system helps to ensure high precision in conformal dose delivery by correcting the rigid displacements and setup errors in treatment geometry in terms of the respective table shifts [3,4]. The vital role of kV CBCT is not limited only to image guided radiotherapy, but is also extended in the determination of non-rigid anatomical transformations viz., change in body contour, tumor shrinkage or growth, and variation in organ filling [5] during the course of treatment. Currently, kV CBCT images are utilized effectively to predict the deviations in the delivered dose distributions. This image data is a promising tool to aid clinical decision making when the physician has to choose between the options of either re-planning or continuing the same plan [6].

Several reports in literature have emphasized the importance of image guided adaptive radiotherapy (IGART) as a part of clinical practice to enhance the therapeutic ratio [7–10]. In most circumstances, acquisition of repeat CT (re-CT) has been shown to be the key requisite to perform the IGART. There are a few practical considerations and challenges in implementing re-CT based IGART in the routine clinical setting, due to the repetition of the entire chain of processes involved in radiotherapy viz., simulation, contouring, dose calculation and pre-treatment dosimetric verification. Another practical concern in re-CT based IGART is the increased financial burden on the treating institution (due to the additional cost of re-imaging and re-planning) [11]. Additionally, each re-CT demands additional work inputs in terms of time and labor from the clinical staff, physicist and physician involved in the procedure, and also decrease the patient throughput [11].

Many investigators have employed kV CBCT images for re-optimization (or re-planning) purposes in order to address the issues related with re-CT [12–15]. Though these images provide appropriate “reconstruction field-of-view” (recon-FOV) of 45 cm, the “longitudinal field-of-view” (longi-FOV) is limited to a mere 16 cm [16–19] which is clinically inadequate. More specifically, this limitation results in situations such as mapped structures falling beyond the longi-FOV of single CBCT when adapting inter-fraction changes through CT-CBCT

---

* Corresponding author.
E-mail addresses: raficmphy@gmail.com, raficmphy@cmcvellore.ac.in (K.M. Rafic), paul@cmcvellore.ac.in (B.P. Ravindran).

https://doi.org/10.1016/j.ejmp.2019.03.007
Received 12 July 2018; Received in revised form 6 March 2019; Accepted 9 March 2019

registration. In addition, dose calculation with CBCT is complex unlike conventional CT, due to their inaccuracies in Hounsfield Units (HU) [20–24], thereby restricting its potential use in IGART.

The present study describes the practical usefulness of CBCT with extended longi-FOV ($CBCT_{eLFOV}$) for IGART in the clinical setting [19]. Initially, $CBCT_{eLFOV}$ image sets have been carefully validated by evaluating the image geometry, spatial resolution and HU accuracy using a Catphan phantom. Subsequently, the end-to-end workflow of two patients who underwent IGART with re-CT has been compared with $CBCT_{eLFOV}$-based IGART for clinical evaluation. Finally, this study has also been extended to show the efficacy of $CBCT_{eLFOV}$ image data in deformable registration for use in IGART.

2. Materials and methods

2.1. CBCT acquisition parameters and geometry

CBCT images have been acquired using a Clinac2100C/D linear accelerator equipped with On-Board Imager® (OBI) kV imaging system (Varian Medical systems, Palo Alto, CA), having fixed acquisition parameters viz., 125 kVp, 80 mA and 684 mAs with a matrix size of 512 × 512 pixels and slice thickness of 2 mm. The CBCT images of the phantom and patient were acquired with half-fan acquisition geometry with half-bowtie filter configuration. In this acquisition mode, the OBI system acquires 600–700 partially-covered projection images over a gantry rotation of 360°.

2.2. Dual-scan CBCT fusion strategy

Two CBCT images were acquired with linear translations of the couch (15 cm shift in the longitudinal direction with respect to the first couch position that results in a 1 cm penumbral overlap) along the patient plane, and fused into a single DICOM (i.e. $CBCT_{eLFOV}$) set, based on their respective "*TableTopLongitudinalPosition*" DICOM-tag [19] as shown in Fig. 1.

Subsequently, the custom-developed software script, coded in MatLab® (vR2018a, The MathWorks Inc, USA) was used to perform HU averaging in the abutting region (Fig. 2) and to correct the HU values in the high density regions [19].

The resultant $CBCT_{eLFOV}$ image set with 31 cm longitudinal projection was then assigned with the same unique identifiers (UID) viz., *StudyInstanceUID*, *SeriesInstanceUID* and *FrameOfReferenceUID* and a *SeriesNumber* tag (in their DICOM header) as those of the first image series. Furthermore, the *InstanceNumber* and *ImagePositionPatient* DICOM entities have also been assigned in line with the first series, in order to identify each slice and the centre of the first voxel transmitted in the image.

2.3. Validation of $CBCT_{eLFOV}$ image data

The validation of the overlapping slices of $CBCT_{eLFOV}$ were carried out by evaluating the spatial resolution using the CTP528 module of the Catphan-504 phantom (The Phantom Laboratory, Greenwich, NY) which consists of 21-line pairs per centimeter test gauge [25]. Also, the scanned slice geometry, misalignment errors and HU accuracy were evaluated using the CTP404 test module of the same phantom. The CTP404 module consists of two pairs of 23° wire ramps (one pair oriented parallel to the x-axis and the other to the y-axis) and seven density inserts viz., Air ($0\,g/cm^3$), Teflon® ($2.16\,g/cm^3$), Derlin® ($1.42\,g/cm^3$), Acrylic ($1.18\,g/cm^3$), polystyrene ($1.03\,g/cm^3$), low density polyethylene (LDPE, $0.92\,g/cm^3$) and polymethylpentene (PMP, $0.83\,g/cm^3$) (25), as shown in Fig. 3.

The geometric accuracy of each slice was determined using line profile analysis taken across the fused wire ramp objects of CTP404 module. The thickness of the slices was verified by taking the product of full width at half maximum HU values (HU_{FWHM}) with a factor 0.4245 (= tan 23°) as stated in Eqs. (1) and (2).

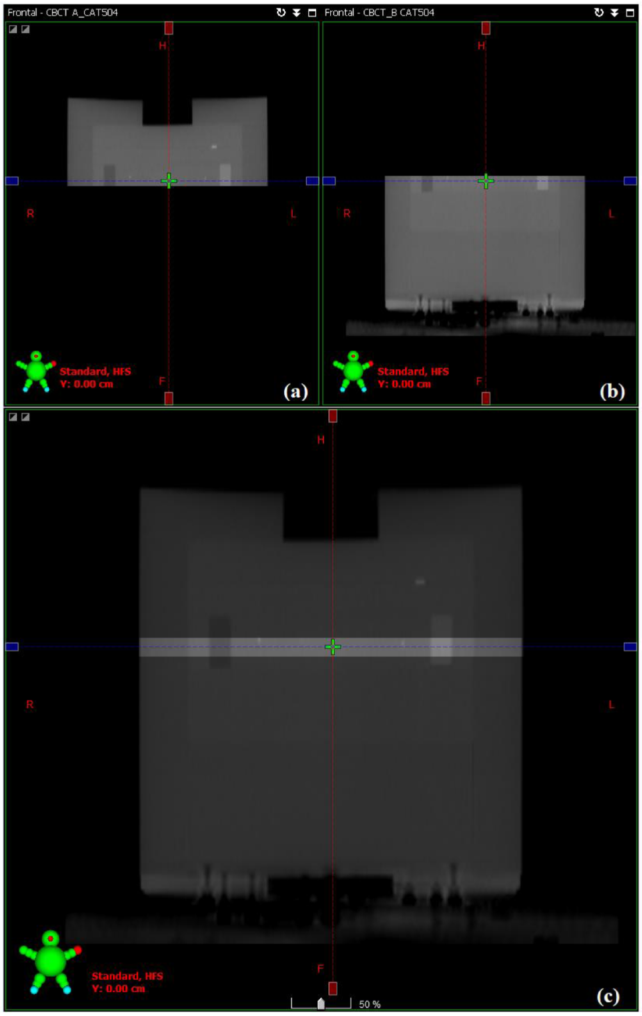

Fig. 1. Coronal images of Catphan-504. (a) First CBCT scan (b) Second CBCT scan with 15 cm longitudinal table shift and (c) fused CBCT ($CBCT_{eLFOV}$). The cross-hairs and highlighted regions indicate the central slice and the overlapping region at CTP404 test module respectively.

$$HU_{FWHM} = 0.5(HU^{BG}_{Peak}) + HU_{BG} \quad (1)$$

$$S^{h}_{f}(mm) = HU_{FWHM} * \tan 23^{O} \quad (2)$$

where, HU^{BG}_{Peak} (in Eq. (1)) is the peak HU value minus mean background HU (HU_{BG}). The letters 'h' and 'f' used in Eq. (2) stand for head and foot directions respectively, which denote the slice numbers in the overlap (Fig. 2).

The possible misalignments as illustrated in Fig. 4 were managed effectively by obtaining an optimum registration between identical slices in the overlap prior to the fusion. All the test results have been validated with care, in comparison with reference CBCT data ($CBCT_{ref}$) which refers to the routine CBCT acquired at the same time with standard longi-FOV of 16 cm.

2.4. Patient simulation and dose calculation

Paradigms of clinical scenarios illustrating the end-to-end VMAT treatment workflow of two patients who underwent IGART with re-CT were also evaluated using $CBCT_{eLFOV}$ image sets. The initial planning CT (initial-pCT) images of the patients were acquired with 500 mm recon-FOV, 3 mm slice thickness and fixed exposure parameters specific to imaging site (120 kVp and 270 mA for the pelvic scan and 120 kVp

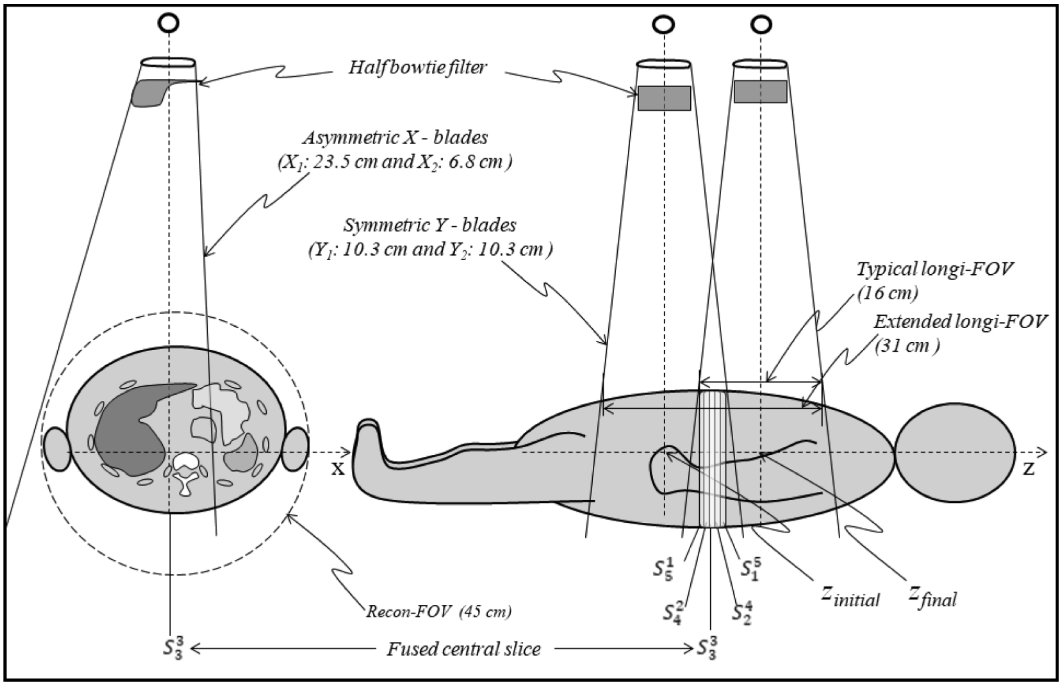

Fig. 2. Schematic (not to scale) illustrating the transversal and side view of half-fan CBCT acquisition geometry used for extended longi-FOV localization.

and 200 mA for the head and neck scan) using Biograph True Point HD CT scanner (Siemens Healthineers, Erlangen, Germany) and transferred to the Eclipse™ treatment planning system (TPS) (v13.7, Varian Medial Systems, Palo Alto, CA) for structure delineation and dose calculation.

2.4.1. *Study I (Abdomen and pelvis)*

In this study, a female patient diagnosed with cervical carcinoma with paraaortic nodal recurrence was investigated. As part of the treatment simulation, the patient who was immobilized in the supine position with a whole body Vac-Lok™ (CIVCO Radiotherapy, Orange City, IA), underwent oral and intravenous contrast administration prior to the imaging. The initial-pCT was acquired from the level of diaphragm to mid-thigh and exported to Eclipse TPS. The gross tumor volume (GTV) was the paraaortic lymph node (T_{12} to L_4) which was radiologically identified on the initial-pCT image set. The clinical target volume (CTV) was created by adding an asymmetric margin (0.5–1 cm) to the GTV. The planning target volume (PTV) included a symmetric margin of 5 mm to the CTV to account for the geometric and setup uncertainties as per the institutional protocol. Additionally, organs-at-risk (OARs) viz., kidneys, bowel bag, and spinal cord were delineated.

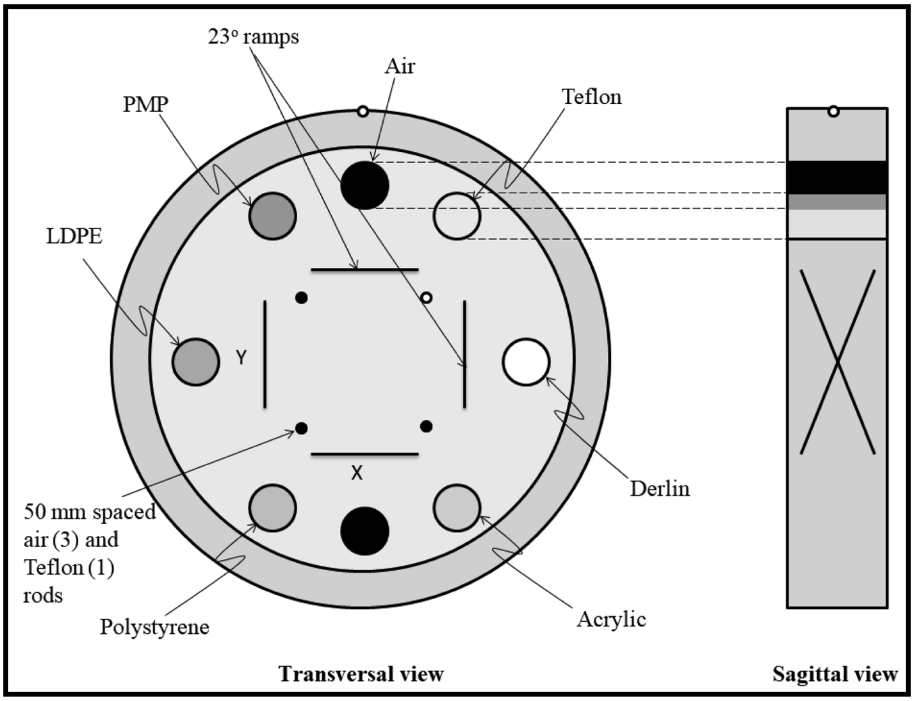

Fig. 3. Schematic of CTP404 test module of Catphan-504 phantom used for scanned slice geometry and HU analysis.

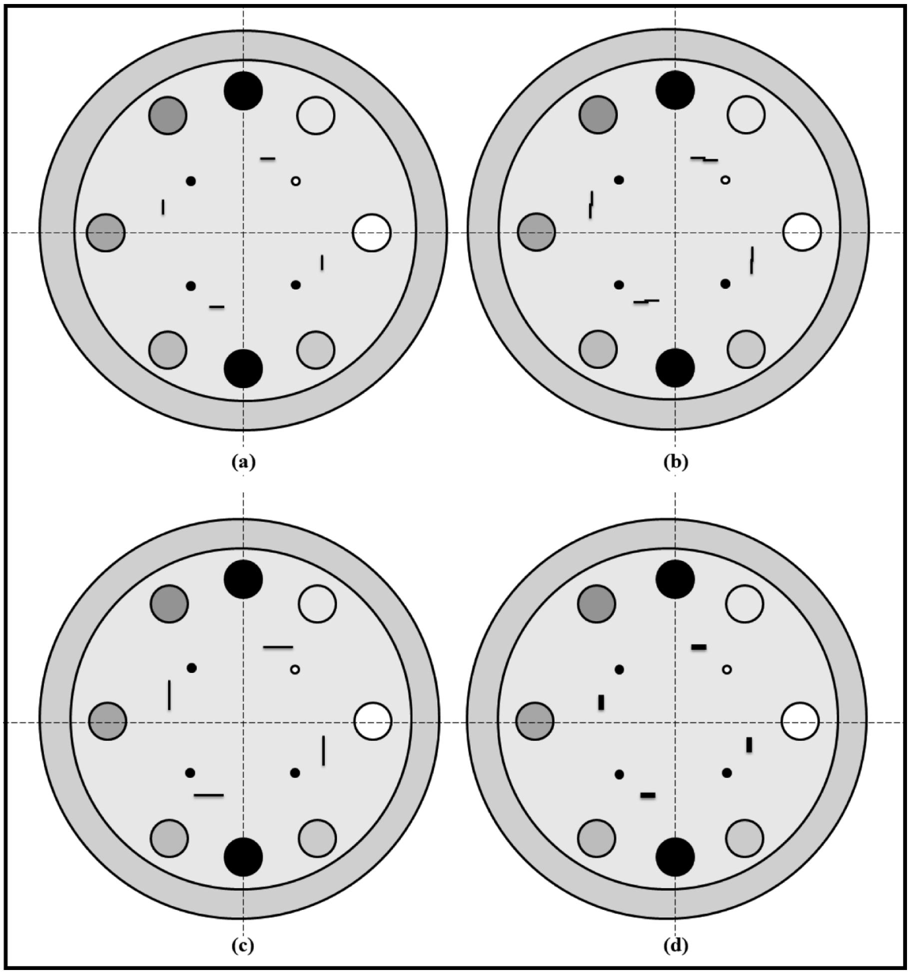

Fig. 4. An example illustrating the fused identical slices in the overlap. (a) Correct alignment, (b, c and d) incorrect alignments with shift in the diagonal, lateral and vertical directions respectively.

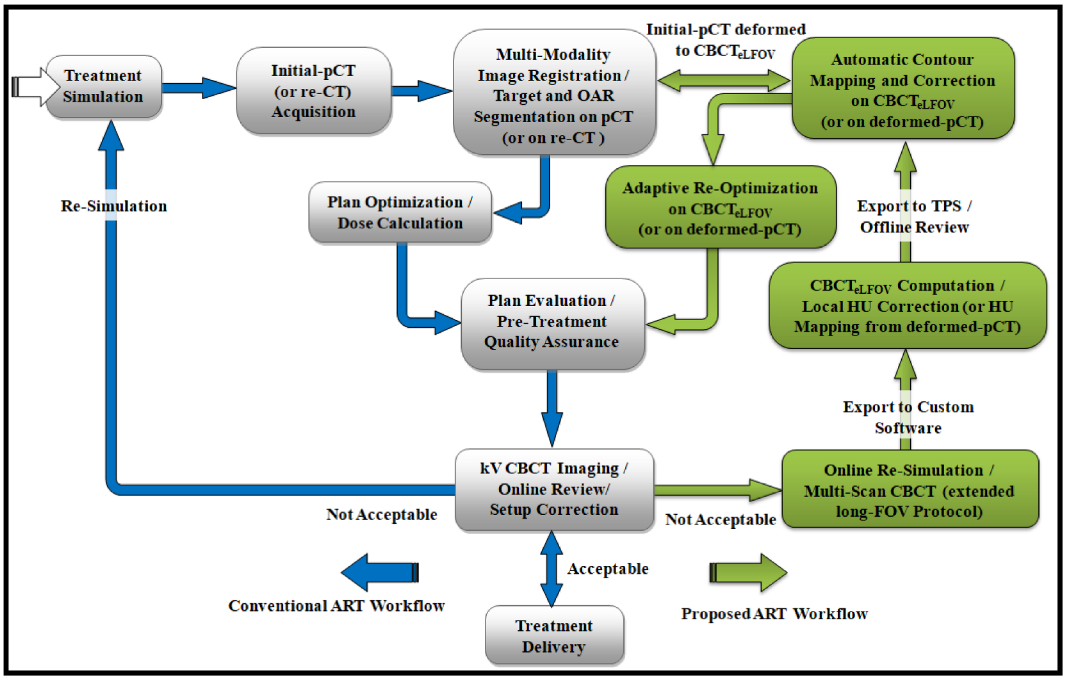

Fig. 5. An overview of conventional (blue arrow) and proposed IGART workflow (green arrow) diagram. (For interpretation of the references to colour in this figure legend, the reader is referred to the web version of this article.)

Table 1

Scanned slice geometry, spatial resolution and HU comparison between CBCT$_{ref}$ and CBCT$_{eLFOV}$.

Slice Geometry (cm)			High Resolution (line pair/cm)		Sensitometry (HU)		
Slice No.	CBCT$_{ref}$ (x/y)	CBCT$_{eLFOV}$ (x/y)	CBCT$_{ref}$	CBCT$_{eLFOV}$	Insert (HU range*)	CBCT$_{ref}$	CBCT$_{eLFOV}$
S_5^1	0.21/0.22	0.23/0.22	4	4	Air (−1046: −986)	−994 ± 6	−998 ± 5
S_4^2	0.23/0.22	0.22/0.22	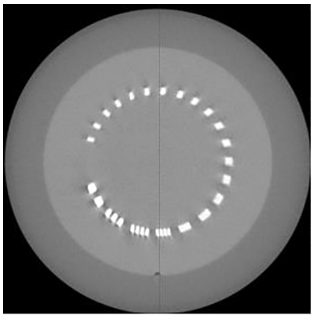	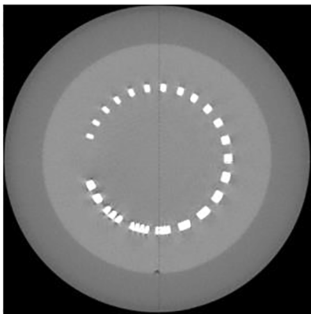	Teflon (941: 1060)	998 ± 10	1036 ± 11
S_3^3	0.24/0.22	0.25/0.24			Derlin (344: 387)	345 ± 7	360.3 ± 10
S_2^4	0.25/0.22	0.24/0.25			Acrylic (92: 137)	122 ± 7	135 ± 8
S_1^5	0.22/0.22	0.25/0.25			Polystyrene (−65: −29)	−37 ± 7	−36 ± 7
–					LDPE (−121: −87)	−97 ± 6	−91 ± 7
					PMP (−220: −172)	−189 ± 6	−184 ± 8

* Catphan-504 manual (The Phantom Laboratory, Greenwich, NY).

2.4.2. Study II (Head and neck)

In this study, a male patient diagnosed with nasopharyngeal carcinoma was investigated. During simulation, the patient was immobilized in the supine position using a Thermoplastic mask (Orfit Industries, Wijnegem, Belgium) and the initial-pCT images were acquired from the level of the vertex to the sternal angle with intravenous contrast. The GTV defined in this study was delineated using PET-CT fusion. While the high-risk CTV (CTV$_{66\ Gy}$) included the pre-induction GTV in the nasopharynx and gross nodal disease with a 5 mm symmetric margin, the low-risk CTV (CTV$_{59.4\ Gy}$) included the areas of potential microscopic disease around the primary as well as the uninvolved bilateral lower neck nodes. Besides, both the PTV structures viz., PTV$_{66\ Gy}$ and PTV$_{59.4\ Gy}$ were created with a symmetric margin of 5 mm around CTV$_{66\ Gy}$ and CTV$_{59.4\ Gy}$ respectively, to account for delivery uncertainties. The PTV structures were adjusted in such a way that they did not extend either outside the body contour or inside the critical OARs, especially the spinal cord and brain stem.

2.5. Adaptive re-simulation and re-optimization

In study I (abdomen and pelvic site), significant loss of body mass resulted in an undesirable difference in the upper quadrant of the abdominal region in the online rigid registration. On the other hand, registration results of the normal tissues and bone structures in the lower quadrant were in contrast to those in the upper quadrant, where optimum matches between the initial-pCT and CBCT were observed. Owing to this unusual observation, the treatment was interrupted (in the 4th week) and the patient underwent re-CT with same immobilization. Similarly, online re-simulation was performed to acquire CBCT$_{eLFOV}$ images of the patient (on the table treatment position). At first, the target and OAR structures and beam centre co-ordinates from the initial-pCT were mapped on to re-CT and CBCT$_{eLFOV}$ through rigid registration. The structural changes were updated as required on both the image sets independently by the same physician, to avoid interobserver uncertainties. Subsequently, the original plan control point parameters viz., monitor units and multileaf collimator geometry (as a function of dose rate, gantry angle and gantry speed) were imported and the dose re-calculation was performed. This procedure revealed the actual dosimetric scenario of the patient treatment when the same plan is continued. In this study, five major structures viz., PTV, CTV, kidneys (right and left) and bowel bag were chosen for plan evaluation. Finally, to account for the contour changes, adaptive re-optimization was computed on both re-CT and CBCT$_{eLFOV}$ image sets.

A similar investigation was also performed for the patient with head and neck cancer in study II. The factor that interrupted treatment (in the 5th week) was primarily a setup error due to irreproducible spine geometry at the neck region. For this patient, minor reduction in body mass and nodal shrinkage were also observed in the online rigid registration. This case selection was made to test the dosimetric impact of setup uncertainty during course of the treatment. In order to address the same, a new thermoplastic mask immobilization was used. The re-CT and CBCT$_{eLFOV}$ image sets were acquired as described in study I. The structure sets (and beam centre co-ordinates) were then mapped and updated on both data sets, and the dose re-calculations were generated. In this study, the targets and vital OARs viz., PTV$_{66\ Gy}$, PTV$_{59.4\ Gy}$, CTV$_{66\ Gy}$, CTV$_{59.4\ Gy}$, parotid (left and right), spinal cord, brainstem and mandible were analyzed in plan evaluation.

Though the primary cause of treatment interruption was different for the two studies as stated above, an identical re-planning workflow was followed to test the potential of CBCT$_{eLFOV}$ guided adaptive radiotherapy. For both patients, the adaptive VMAT re-plan computed on re-CT was utilized to complete the remaining course of treatment.

2.6. Modified demons algorithm and deformed initial-pCT for IGART

In the present study, the efficacy of modified demons deformable registration algorithm (MDDR) (v13.6, Eclipse SmartAdapt, Varian Medical Systems, Palo Alto, CA) for IGART was also investigated. The differences in image intensity (or the HU value) between the source (initial-pCT) and target (re-CT or CBCT$_{eLFOV}$) images are the driving forces for the demon algorithms. The basic concept behind this algorithm is that the non-rigid transformation of an object can be described by a diffusion equation [26]. Solving this equation is an iterative process in which the spatial transformation of target image voxels are scaled with respect to the same voxels in the source image, so that the latter can be morphed and aligned voxel by voxel into the former in image space.

The MDDR approach presented in our study consists of two distinct deformed initial-pCT image sets, of which one was deformed to re-CT and the other was deformed to CBCT$_{eLFOV}$. Each deformed data set shares the same frame of reference and DICOM UIDs as those of its corresponding target image set. The entire IGART workflow described with re-CT and CBCT$_{eLFOV}$ were also investigated using the deformed data sets. This approach was proposed in order to use the HU values of the conventional CT (deformed initial-pCT) image sets for dose calculation, as it does not require any HU correction and can be utilized

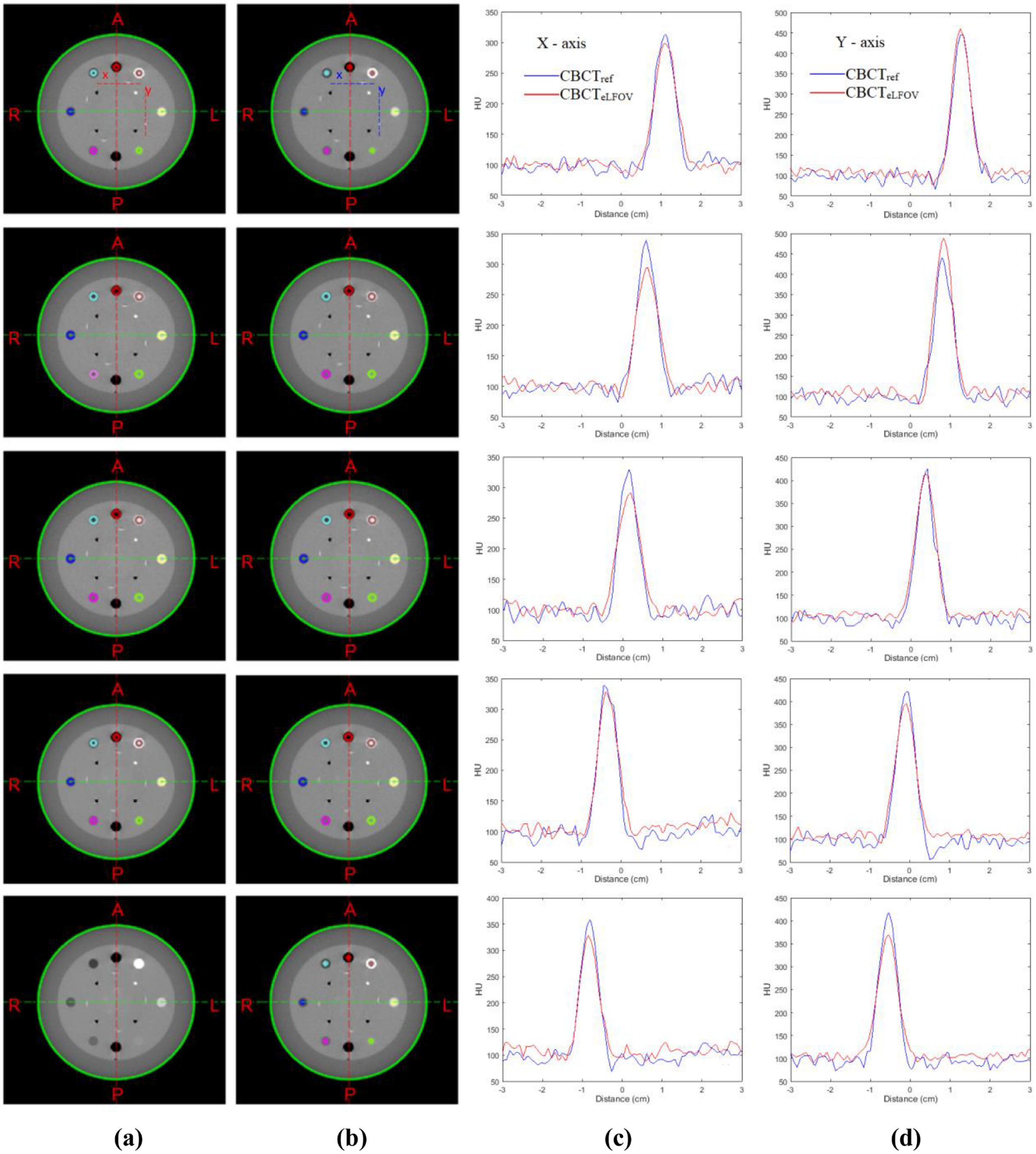

Fig. 6. All five fused slices of CTP404 module with exact ramp alignment in comparison with the corresponding slices of $CBCT_{ref}$ and the line profiles across the ramps (indicated by dotted lines on the first slice). (a) $CBCT_{eLFOV}$, (b) $CBCT_{ref}$, (c) and (d) line profiles along X – axis and Y – axis ramp respectively.

directly for the calculation of dose.

We have also included further studies to describe the usability of $CBCT_{eLFOV}$ for deformable registration and for IGART. The complete overview of conventional re-CT and proposed $CBCT_{eLFOV}$ (or initial-pCT deformed to $CBCT_{eLFOV}$) based IGART workflow is presented in Fig. 5.

2.7. Similarity comparison metric

At first, the centre of mass shift co-ordinates ($CMS_{x,y,z}$) of all the structures delineated in the initial-pCT (original baseline) were recorded and compared with those mapped and updated on the re-CT as well as the $CBCT_{eLFOV}$. Similar evaluation was also made for the structures updated on deformed image sets in comparison with the re-CT (new baseline). Secondly, the volumetric dice-similarity-coefficient (DSC_{VOL}) was used to evaluate the degree of association in spatial overlap of structures defined among the adaptive image sets (i.e. re-CT, $CBCT_{eLFOV}$, initial-pCT deformed to re-CT and initial-pCT deformed to $CBCT_{eLFOV}$). DSC_{VOL} is an important quantitative metric, widely used to test image segmentation accuracy. It pertains to the geometric intersection of two structure volumes normalized to their mean volume, which can be calculated as stated in Eq. (3) [27].

$$DSC_{VOL} \equiv \frac{N(X \cap Y)}{0.5[N(X) + N(Y)]} \quad (3)$$

where, ‘X’ is the structure geometry defined on re-CT (considered as new baseline reference), ‘Y’ is the structure defined on $CBCT_{eLFOV}$ and deformed initial-pCT image sets, and N is the number of voxels. The value of DSC_{VOL} ranges from 0 to 1, that is analogous to “no

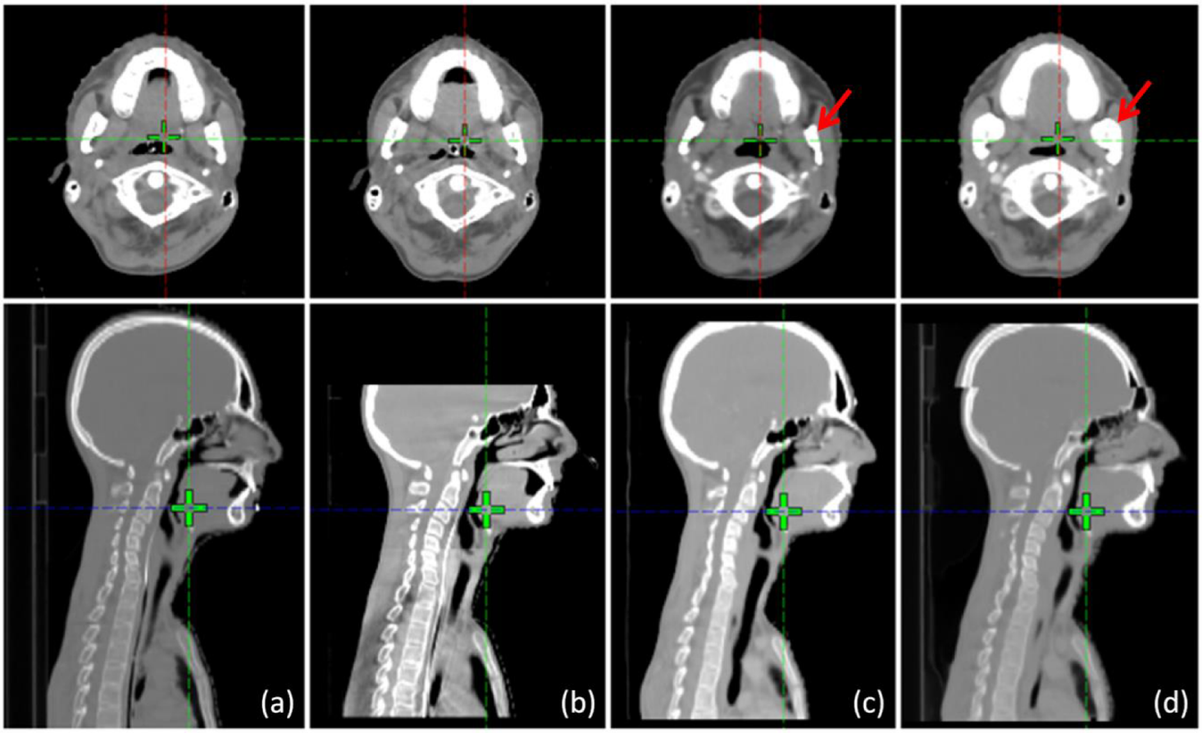

Fig. 7. Axial and sagittal images of head and neck patient. (a) re-CT (a new baseline standard), (b) $CBCT_{eLFOV}$, (c) initial-pCT deformed to re-CT and (d) initial-pCT deformed to $CBCT_{eLFOV}$. (Red arrow indicates less than desirable mandible deformation results of MDDR). (For interpretation of the references to colour in this figure legend, the reader is referred to the web version of this article.)

Table 2
The measure of central tendency of $CMS_{x,y,z}$ and DSC_{vol} before and after contour adaption.

Case ID	pCT vs. re-CT	pCT vs. $CBCT_{eLFOV}$	re-CT vs. $CBCT_{eLFOV}$	re-CT vs. pCT deformed to re-CT	re-CT vs. pCT deformed to $CBCT_{eLFOV}$
			Centre of mass shift (X, Y, Z) in mm		
Study I (mean ± SD (range)	1.7 ± 2.2 (1.0–4.0), 4.1 ± 3.6 (1.0–10.0), 1.4 ± 3.0 (0–7.0)	1.4 ± 2.2 (0.4–3.2), 2.7 ± 3.6 (0.8–8.7), 0 ± 3.0 (0.9–4.7)	0 ± 0 (0–0.1), 0.1 ± 0.1 (0–0.2), 0.3 ± 0.3 (0–0.9)	0.1 ± 0.1 (0–0.1), 0.1 ± 0.1 (0–0.1), 0.3 ± 0.3 (0.3–0.7)	0.8 ± 1.1 (0.1–2.3), 0.3 ± 1.5 (0–2.7), 1.2 ± 2.6 (0.1–2.3)
Study II (mean ± SD (range)	0.7 ± 3.6 (0–8.0), 7.3 ± 2.3 (3.5–10.4), 0.1 ± 4.8 (0.3–9.2)	0.9 ± 3.5 (0.1–7.5), 7.8 ± 3.2 (2.3–11.1), 1.3 ± 4.9 (1.1–8.2)	0.1 ± 0.5 (0.1–1.2), 1.0 ± 1.1 (0–3.1), 1.2 ± 1.5 (0.1–4.6)	0.0 ± 0.2 (0–0.4), 0.3 ± 0.5 (0.1–0.9), 0.8 ± 0.7 (0.1–2.1)	0.2 ± 0.5 (0–1.3), 0.2 ± 0.9 (0–1.7), 0.7 ± 1.3 (0.1–3.1)
			Volumetric dice-similarity-coefficient		
Study I (mean ± SD (range)	0.80 ± 0.06 (0.74–0.89)	0.82 ± 0.05 (0.77–0.88)	0.97 ± 0.01 (0.95–0.98)	0.96 ± 0.01 (0.95–0.98)	0.93 ± 0.05 (0.87–0.98)
Study II (mean ± SD (range)	0.56 ± 0.19 (0.28–0.78)	0.54 ± 0.18 (0.28–0.78)	0.89 ± 0.05 (0.81–0.95)	0.94 ± 0.03 (0.90–0.98)	0.94 ± 0.54 (0.83–0.99)

correspondence” and “complete correspondence” respectively.

3. Results

3.1. Slice geometry, spatial resolution and HU analysis

Table 1 compares the slice geometry, spatial resolution and HU values of $CBCT_{eLFOV}$ (where the cone beam overlap occurred) with those of $CBCT_{ref}$. The spatial resolution evaluated at the centre of overlap was found to be identical to that of $CBCT_{ref}$ image set as reported in the same table. The optimally fused five overlapping axial slices of $CBCT_{eLFOV}$ were found to have similar spatial geometry and ramp alignment in comparison with $CBCT_{ref}$ data sets as shown in Fig. 6a and b. A marginal increase in profile widths and decrease in HU^{BG}_{Peak} values were found in the line profiles (across the ramp objects) of $CBCT_{eLFOV}$ when compared with $CBCT_{ref}$, for all the five slices evaluated. Fig. 6c and d illustrate those profiles across both X and Y axes of the ramps. Slice thickness analysis showed that the variation was within ± 0.3 mm, showing good agreement overall. The maximum HU variation observed between $CBCT_{eLFOV}$ and $CBCT_{ref}$ images was $<$ 40 HU that was well within the HU range specified by the manufacturer [25].

3.2. Structure volume comparison

In both case studies, the variations observed in the volumes of target and OAR structures between initial-pCT and re-CT were found to be similar to those observed between initial-pCT and $CBCT_{eLFOV}$.

In study I, the relative difference in structure volumes between re-CT and $CBCT_{eLFOV}$ was found to be within ± 2%. A consistent pattern of results was also observed for all the structures updated on the deformed initial-pCT image sets (i.e. initial-pCT deformed to re-CT and $CBCT_{eLFOV}$ respectively). However, a maximum difference of about 10% that corresponds to an absolute value of 14.5 cc was observed in the right kidney structure, updated on the initial-pCT deformed to $\mathrm{CBCT}_{\mathrm{eLFOV}}$.

In study II, the structure volume comparison showed a similar trend as observed in study I. Further, it was noted that the $\mathrm{CTV}_{59.4\ \mathrm{Gy}}$ and mandible structures updated on the $\mathrm{CBCT}_{\mathrm{eLFOV}}$ and deformed image sets were recorded with greater variation in comparison with re-CT. The axial and sagittal planes of re-CT, $\mathrm{CBCT}_{\mathrm{eLFOV}}$, and initial-pCT deformed to re-CT and $\mathrm{CBCT}_{\mathrm{eLFOV}}$ are presented in Fig. 7.

3.3. Structure similarity comparison

In both the case studies, relatively similar variations were observed in $\mathrm{CMS}_{x,y,z}$ co-ordinates for all the structures updated in re-CT and $\mathrm{CBCT}_{\mathrm{eLFOV}}$ when compared with initial-pCT as summarized in Table 2. In addition, $\mathrm{CMS}_{x,y,z}$ comparison between re-CT vs. $\mathrm{CBCT}_{\mathrm{eLFOV}}$ and re-CT vs. deformed initial-pCT image sets were also found to have a more or less similar tendency (refer Table 2). The overall shift in $\mathrm{CMS}_{x,y,z}$ co-ordinates ranged from 0 to 0.9 mm and 0 to 4.6 mm for studies I and II respectively.

The mean $\mathrm{DSC}_{\mathrm{VOL}}$ measured from the $\mathrm{CBCT}_{\mathrm{eLFOV}}$, initial-pCT deformed to re-CT and initial-pCT deformed to $\mathrm{CBCT}_{\mathrm{eLFOV}}$ in comparison with re-CT (new reference) were found to be 0.97 ± 0.01, 0.96 ± 0.01 and 0.93 ± 0.05 respectively in study I and 0.89 ± 0.05, 0.94 ± 0.03 and 0.94 ± 0.05 respectively in study II as presented in the same table.

3.4. Dosimetric comparison

The dosimetric impact of patient deformation (in Study I) and irreproducible treatment setup (in Study II) were analyzed. The initial-pCT based original plan when imported on the re-CT showed major variations from the planned doses for the target (in study I) and OAR structures (in study II) as illustrated in Fig. 8a and b. More specifically in study II, the spine and brainstem doses were found to have gross deviations which were outside the tolerance limits.

The dosimetric variations in original dose distribution observed using re-CT were also accurately predicted using $\mathrm{CBCT}_{\mathrm{eLFOV}}$ (refer Fig. 9a and b). Moreover, the dose distributions and dose volume histograms (DVHs, as shown in Fig. 9) of adaptive re-plans generated using $\mathrm{CBCT}_{\mathrm{eLFOV}}$ and deformed initial-pCT image sets were also found to be matching well (≤ ± 2%) with re-CT, which are clinically acceptable.

4. Discussion

Early reports of dosimetric feasibility of using CBCT for dose delivery verification and dose calculation [6,10,12,13,20–22,28] have increased the interest in utilizing this imaging modality for IGART. Some authors have also reported improved accuracy in dose calculation with CBCT using appropriate scatter rejection and HU modification strategies [22,29–31]. However, they have not addressed the practical

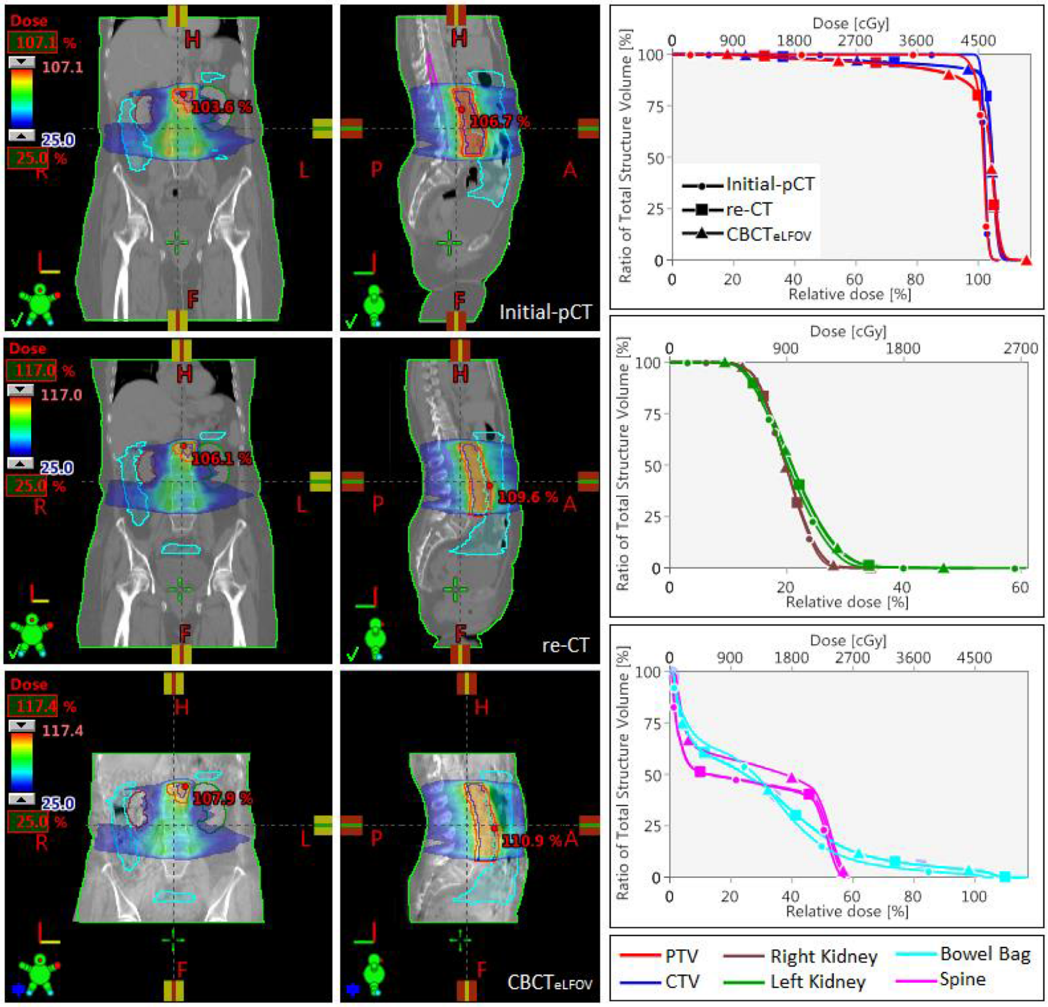

(a)

Fig. 8. Accurate prediction of deviation in the original dose distributions after importing the initial-pCT based treatment plan onto the re-CT and $\mathrm{CBCT}_{\mathrm{eLFOV}}$ and the corresponding dose volume histograms of target and OARs structures. (a) Study I (Abdomen and pelvis) and (b) study II (head and neck).

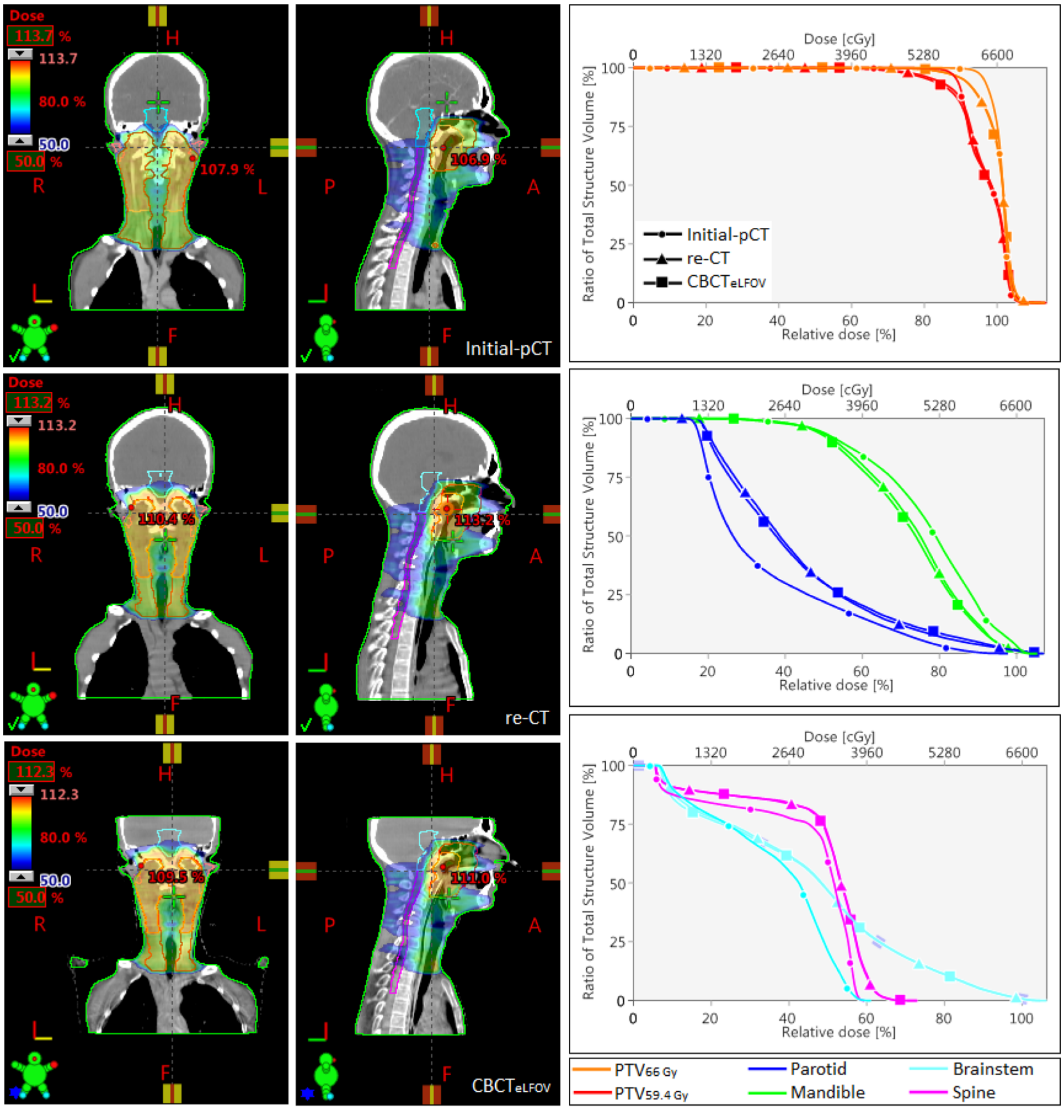

(b)

Fig. 8. (*continued*)

limitation in the longi-FOV of CBCT which is a clinical requisite to perform IGART of head and neck, and pelvic sites with large PTV and regional nodes. In this study, HU-modified CBCT [19] with extended longitudinal projection has been demonstrated as a promising tool for treatment plan evaluation and IGART. This study is expected to complement published research and also to encourage further research into this topic.

The systematic validation methods viz., slice geometry, spatial resolution and line profile analysis described in our study could detect even small inconsistencies present in the fused CBCT$_{eLFOV}$ data (refer Table 1 and Fig. 6). These errors (Fig. 6a and b) are otherwise visually indistinguishable from the CBCT$_{ref}$ in the rigid registration. In general, reconstruction with a large cone angle, penumbral HU averaging with minor misregistration, motion artifacts, couch position and setup uncertainties are all potential causes of image inaccuracy in the overlap [19]. Therefore, a scan length of less than 16 cm each and rigid registration between the identical slice in the overlap region are recommended to minimize them, especially for PTV with a length ≤ 25 cm. With this approach, the resultant CBCT$_{eLFOV}$ data would provide optimum fusion and an adequate margin on either side of the PTV border to compute accurate dose calculations. It is worth mentioning that the marginal differences in slice geometry and HU values do not have an effect on dose calculation. However, images with appropriate spatial information are vital for accurate and consistent interpretation of clinical structures for precise localization and for IGART.

We have utilized a half-fan CBCT mode with a half bowtie filter as the standard acquisition geometry irrespective of the anatomical site, since it offers a maximum recon-FOV of 45 cm with reduced artifacts, compared with the full-fan mode. Therefore, evaluation of the full-fan acquisition mode (recon-FOV ~ 25 cm) with a full bowtie filter to extend the longitudinal projection is beyond the scope of the present study and has hence been excluded. However, we recommend low-dose CBCT with the full-fan mode or planar projection radiographs for image guidance on other days when the CBCT$_{eLFOV}$-based online re-simulation is not required. This will reduce the imaging dose if more than one IGART procedure is to be performed within the planned course of treatment.

Owing to the lack of specific guidelines for comprehensive IGART protocols with CBCT, the CBCT$_{eLFOV}$ approach presented in this study is expected to play a major role in the improvement of IGART practice. In addition, it does not affect the typical clinical time since it can be acquired online as part of pre-treatment image guidance. Nevertheless, it is obvious that one should perform careful validation, calibration and

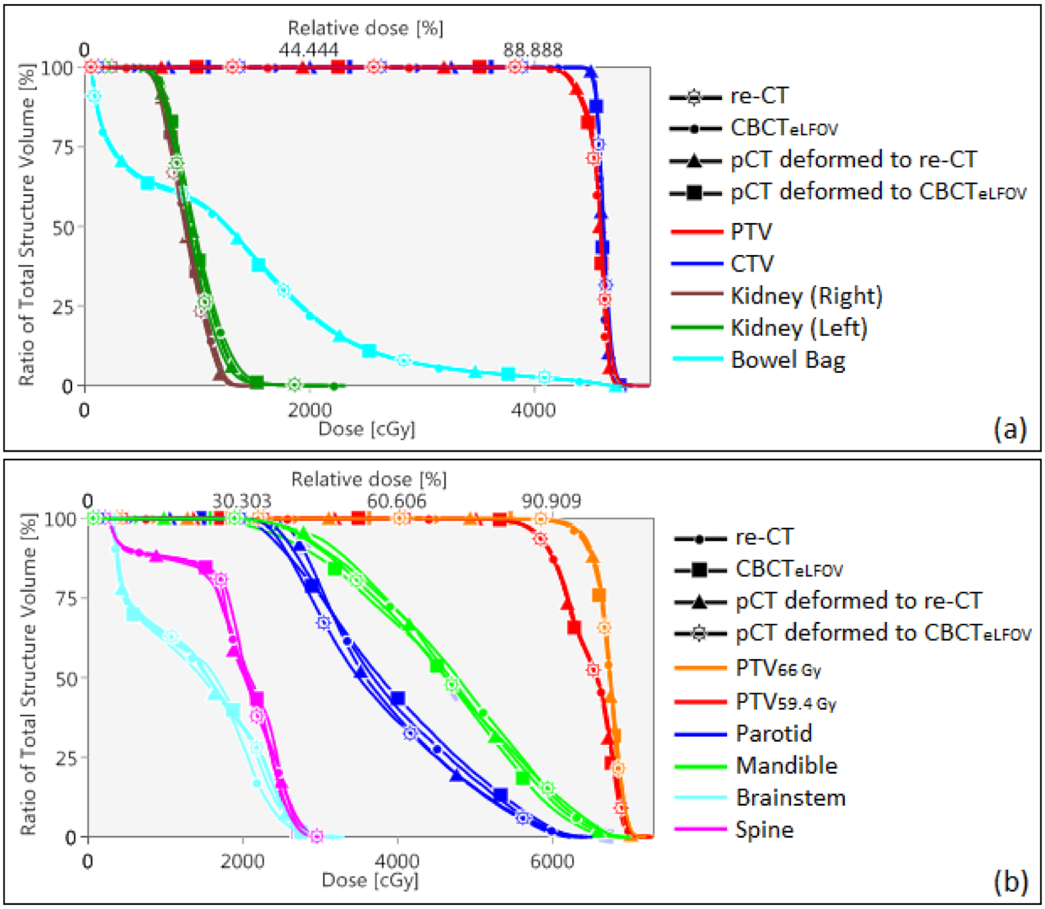

Fig. 9. Plan comparison DVHs computed through adaptive re-optimization procedure showing excellent agreement among adaptive image sets. (a) Study I and (b) Study II.

correction of CBCT HU values, to generate the treatment plans equivalent to conventional CT-based plans.

In this study, minor differences in the delineated structures were observed between re-CT and $\text{CBCT}_{\text{eLFOV}}$ image data. This is due to the relatively inferior contrast visibility and spatial information of CBCT in comparison with contrast-enhanced conventional re-CT. Thus, the GTV volumes mapped from initial-pCT to adaptive data sets were not reduced in size, in order to be on the safer side for loco-regional control as followed by Hansen et al. [11]. The right kidney structure in study I and the mandible structure in study II updated on the initial-pCT deformed to $\text{CBCT}_{\text{eLFOV}}$ recorded major variations. Possible causes could be the excessive reduction in body mass (Study I) and the irreproducible setup (Study II) respectively. Thus, further investigation concerning correlation between the accuracy of deformation with image intensity (different imaging parameters), change in body mass (loss or gain), and difference in rigid registrations would provide more information.

The mean DSC_{vol} and $\text{CMS}_{x,y,z}$ co-ordinates observed from $\text{CBCT}_{\text{eLFOV}}$ images (table 2) were found to have good association with the structures updated on re-CT images. This result showed the efficacy of $\text{CBCT}_{\text{eLFOV}}$ as a promising tool for adaptive plan evaluation. These segmentation metrics have a specific relationship with the dosimetric outcome. Therefore, adapting (or recording) them in addition to the beam centre shift assessment during online registration protocol, provides useful insights about anatomical association (or dissociation). If such metrics are added in the treatment console registration algorithms, then one can use them as an action level indicator for offline/online IGART in the future.

In most cases, the entire bony anatomy in initial-pCT did not match exactly with the $\text{CBCT}_{\text{eLFOV}}$. This is due to patient deformation and the irreproducible treatment setup within the planned course of treatment. Therefore, the practical usefulness of extended deformation (i.e. initial-pCT deformed to $\text{CBCT}_{\text{eLFOV}}$) using $\text{CBCT}_{\text{eLFOV}}$ for IGART was also presented in this study. Moreover, the image intensities (or HU values) of the initial-pCT and $\text{CBCT}_{\text{eLFOV}}$ images are relatively consistent, to permit tracking of spatial displacements of similar voxels and to deform (or transform) them accurately in the image space. The MDDR algorithm in Eclipse TPS was found to satisfactorily transform the initial-pCT image matrix for most of the target structures. However, it yielded less than desirable deformation results for a few structures in both the studies (refer Fig. 7), due to the large variations in body mass and treatment setup. One important finding is that there was no influence on the dose distribution when the original plan was re-optimized with updated structures set (refer Fig. 9). Hence, deformed image data (initial-pCT deformed to $\text{CBCT}_{\text{eLFOV}}$) sharing the same frame-of-reference of $\text{CBCT}_{\text{eLFOV}}$ are also expected to be a potential tool for dosimetric plan evaluation and IGART. Moreover, the HU values of deformed pCT images can also be directly used for adaptive dose calculation. On the other hand, it is vital to perform careful validation of the accuracy of the deformation prior to its clinical use. As the errors in deformed CT image sets are the cause of the dose deviations and inaccurate dose calculations [32], it would be more appropriate to utilize the soft-tissue data of $\text{CBCT}_{\text{eLFOV}}$ to accurately predict the dosimetric consequences. $\text{CBCT}_{\text{eLFOV}}$ image guidance provides a complete picture of the actual dose delivered to the patient. Moreover, it facilitates the physician to make realistic clinical decisions during the planned course of treatment. This method can also be easily implemented in any clinic equipped with integrated kV CBCT facility on the linear accelerator with minor changes in the DICOM script.

5. Conclusion

This study successfully demonstrated the practicability of using the $\text{CBCT}_{\text{eLFOV}}$ image sets for adaptive plan verification and IGART. The $\text{CBCT}_{\text{eLFOV}}$ images were comprehensively validated using systematic evaluation metrics and found to be suitable for clinical use. $\text{CBCT}_{\text{eLFOV}}$ image guidance is clinically apt for localizing large target volumes in high precision radiotherapy. It is also effective in the management of inter-fraction geometric uncertainties and serves as a guide to deform the initial-pCT with extended longitudinal projection. In addition, it helps in setting up a new reference (baseline) image without affecting the overall machine throughput and clinical workload which are the main concerns of performing routine IGART. The comparable dosimetric outcome observed between re-CT and $\text{CBCT}_{\text{eLFOV}}$ validate the use of the latter as a suitable as well as a viable alternative to perform IGART with regular frequency.

Conflict of interest

None.

Acknowledgements

The authors would like to thank Dr. Isobel Swamidasan, Professor and Ms. Amala, Medical Physicist, for their help in proof reading this manuscript. The research work presented in this manuscript is a part of the Ph.D. Thesis of The Tamil Nadu Dr.M.G.R. Medical University, Chennai, India. This Project was funded in part by Atomic Energy Regulatory Board (AERB/CSRB/Proj.No.65/02/2016), India.

Appendix A. Supplementary data

Supplementary data to this article can be found online at https://doi.org/10.1016/j.ejmp.2019.03.007.

References

[1] Jaffray DA, Siewerdsen JH, Wong JW, Martinez AA. Flat-panel cone-beam computed tomography for image-guided radiation therapy. Int J Radiat Oncol Biol Phys 2002;53(5):1337–49.
[2] Garayoa J, Castro P. A study on image quality provided by a kilovoltage cone-beam computed tomography. J Appl Clin Med Phys 2013;14(1) Available from: http://www.jacmp.org/index.php/jacmp/article/view/3888.
[3] Thilmann C, Nill S, Tücking T, Höss A, Hesse B, Dietrich L, et al. Correction of patient positioning errors based on in-line cone beam CTs: clinical implementation and first experiences. Radiat Oncol Lond Engl 2006 May;24(1):16.
[4] Dzierma Y, Beyhs M, Palm J, Niewald M, Bell K, Nuesken F, et al. Set-up errors and planning margins in planar and CBCT image-guided radiotherapy using three different imaging systems: a clinical study for prostate and head-and-neck cancer. Phys Medica Eur J Med Phys 2015;31(8):1055–9.
[5] Heijkoop ST, Langerak TR, Quint S, Mens JWM, Zolnay AG, Heijmen BJM, et al. Quantification of intra-fraction changes during radiotherapy of cervical cancer assessed with pre- and post-fraction Cone Beam CT scans. Radiother Oncol 2015 Dec 1;117(3):536–41.
[6] Ding GX, Duggan DM, Coffey CW, Deeley M, Hallahan DE, Cmelak A, et al. A study on adaptive IMRT treatment planning using kV cone-beam CT. Radiother Oncol 2007;85(1):116–25.
[7] Wu C, Jeraj R, Olivera GH, Mackie TR. Re-optimization in adaptive radiotherapy. Phys Med Biol 2002;47(17):3181.
[8] Yan D, Vicini F, Wong J, Martinez A. Adaptive radiation therapy. Phys Med Biol 1997;42(1):123–32.
[9] Lamb J, Cao M, Kishan A, Agazaryan N, Thomas DH, Shaverdian N, et al. Adaptive radiation therapy: implementation of a new process of care. Cureus 2018;9.
[10] Nijkamp J, Pos FJ, Nuver TT, de Jong R, Remeijer P, Sonke J-J, et al. Adaptive radiotherapy for prostate cancer using kilovoltage cone-beam computed tomography: first clinical results. Int J Radiat Oncol 2008;70(1):75–82.
[11] Hansen EK, Bucci MK, Quivey JM, Weinberg V, Xia P. Repeat CT imaging and replanning during the course of IMRT for head-and-neck cancer. Int J Radiat Oncol 2006;64(2):355–62.
[12] Yang Y, Schreibmann E, Li T, Wang C, Xing L. Evaluation of on-board kV cone beam CT (CBCT)-based dose calculation. Phys Med Biol 2007 Feb 7;52(3):685–705.
[13] Rong Y, Smilowitz J, Tewatia D, Tomé WA, Paliwal B. Dose calculation on KV cone beam CT images: an investigation of the hu-density conversion stability and dose accuracy using the site-specific calibration. Med Dosim 2010;35(3):195–207.
[14] Usui K, Ichimaru Y, Okumura Y, Murakami K, Seo M, Kunieda E, et al. Dose calculation with a cone beam CT image in image-guided radiation therapy. Radiol Phys Technol 2013 Jan;6(1):107–14.
[15] Barateau A, Garlopeau C, Cugny A, Figueiredo BHD, Dupin C, Caron J, et al. Dose calculation accuracy of different image value to density tables for cone-beam CT planning in head & neck and pelvic localizations. Phys Medica Eur J Med Phys 2015;31(2):146–51.
[16] Siewerdsen JH, Daly MJ, Bakhtiar B, Moseley DJ, Richard S, Keller H, et al. A simple, direct method for x-ray scatter estimation and correction in digital radiography and cone-beam CT: X-ray scatter correction. Med Phys 2005;33(1):187–97.
[17] Zheng D, Lu J, Jefferson A, Zhang C, Wu J, Sleeman W, et al. A protocol to extend the longitudinal coverage of on-board cone-beam CT. J Appl Clin Med Phys 2012;13(4) Available from: http://jacmp.org/index.php/jacmp/article/view/3796.
[18] Elstrøm UV, Muren LP, Petersen JBB, Grau C. Evaluation of image quality for different kV cone-beam CT acquisition and reconstruction methods in the head and neck region. Acta Oncol 2011;50(6):908–17.
[19] Rafic KM, Amalan S, Timothy Peace BS, Ravindran BP. Extended localization and adaptive dose calculation using HU corrected cone beam CT: phantom study. Rep Pract Oncol Radiother 2018;23(2):126–35.
[20] Richter A, Hu Q, Steglich D, Baier K, Wilbert J, Guckenberger M, et al. Investigation of the usability of conebeam CT data sets for dose calculation. Radiat Oncol 2008;3(1):42.
[21] Fu W, Yang Y, Yue N, Heron D, Huq M. SU-FF-J-02: a cone beam CT—guided online plan modification technique to correct interfractional anatomic changes for prostate cancer IMRT treatment. Med Phys 2007;34(6):2368.
[22] van Zijtveld M, Dirkx M, Heijmen B. Correction of conebeam CT values using a planning CT for derivation of the “dose of the day”. Radiother Oncol 2007;85(2):195–200.
[23] Juh R, Back G, Ahn S, Kim J, Suh T. SU-GG-I-23: a comparison of adaptive radiotherapy treatment planning between planning CT and KVCBCT. Med Phys 2008;35(6):2647.
[24] Stock M, Pasler M, Birkfellner W, Homolka P, Poetter R, Georg D. Image quality and stability of image-guided radiotherapy (IGRT) devices: a comparative study. Radiother Oncol J Eur Soc Ther Radiol Oncol 2009;93(1):1–7.
[25] Catphan® 504 Manual. The Phantom Laboratory, Inc., Greenwich, NY; 2013.
[26] Thirion J-P. Image matching as a diffusion process: an analogy with Maxwell’s demons. Med Image Anal 1998;2(3):243–60.
[27] Veiga C, McClelland J, Moinuddin S, Lourenço A, Ricketts K, Annkah J, et al. Toward adaptive radiotherapy for head and neck patients: feasibility study on using CT-to-CBCT deformable registration for “dose of the day” calculations. Med Phys 2014;41(3):031703.
[28] Yoo S, Yin F-F. Dosimetric feasibility of cone-beam CT-based treatment planning compared to CT-based treatment planning. Int J Radiat Oncol 2006;66(5):1553–61.
[29] Fotina I, Hopfgartner J, Stock M, Steininger T, Lütgendorf-Caucig C, Georg D. Feasibility of CBCT-based dose calculation: comparative analysis of HU adjustment techniques. Radiother Oncol 2012;104(2):249–56.
[30] Thing RS, Bernchou U, Hansen O, Brink C. Accuracy of dose calculation based on artefact corrected Cone Beam CT images of lung cancer patients. Phys Imaging Radiat Oncol 2017;1:6–11.
[31] Onozato Y, Kadoya N, Fujita Y, Arai K, Dobashi S, Takeda K, et al. Evaluation of on-board kV cone beam computed tomography-based dose calculation with deformable image registration using hounsfield unit modifications. Int J Radiat Oncol 2014;89(2):416–23.
[32] Poon M, Holborn C, Cheng KF, Fung WWK, Chiu G. Evaluation of deformed image-based dose calculations for adaptive radiotherapy of nasopharyngeal carcinoma. Med Dosim 2017;42(4):273–81.